Supplementary Information

Toward triggered generation of indistinguishable single-photons from $MoTe_2$ quantum emitters

Paweł Wyborski,[1] Athanasios Paralikis,[1] Pietro Metuh,[1] Martin A. Jacobsen,[1] Christian C. Ruiz Madera,[1,2] Niels Gregersen,[1] and Battulga Munkhbat[1,†]

[1] *Department of Electrical and Photonics Engineering, Technical University of Denmark, 2800 Kongens Lyngby, Denmark*

[2] *NanoPhoton - Center for Nanophotonics, Technical University of Denmark, 2800 Kgs. Lyngby, Denmark*

[†]email: bamunk@dtu.dk

Contents

Supplementary Notes

Supplementary Note 1: Bilayer $MoTe_2$ sample preparation.

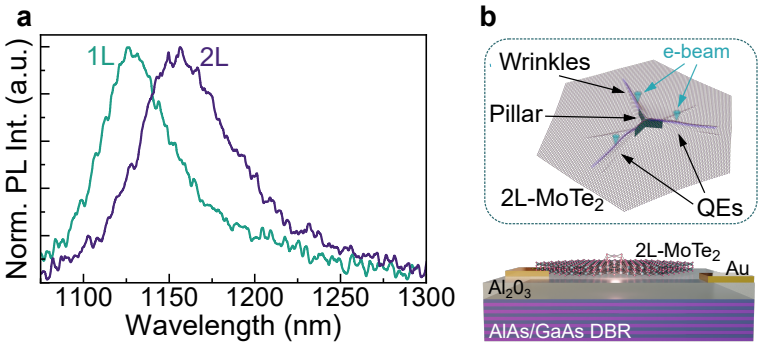

Supplementary Figure 1: **(a)** Photoluminescence spectra of exemplary 1L and 2L $MoTe_2$ flakes on a PDMS stamp measured at T $\sim$ 300 K, using a typical µPL setup. **(b)** A sketch of a $MoTe_2$ flake transferred on top of a pillar, forming nanowrinkles which are subsequently irradiated by an e-beam, used for quantum emitter creation. Additional sketch of the full sample, including the substrate consisting of distributed Bragg reflector, Al_2O_3 layer, pillar, and gold electrodes.

$MoTe_2$ flakes were initially exfoliated from a bulk crystal (HQ Graphene) using the scotch-tape method [1]. Subsequently, they were deposited onto a polydimethylsiloxane (PDMS) stamp prepared on a glass slide. The bilayers were identified via room-temperature photoluminescence (RT PL) measurements using a custom µPL setup (Nikon 50× objective, NA = 0.8) and a 650 nm above-band CW laser excitation source (PicoQuant, LDH-D-C-650). The selected flakes exhibited PL spectra with peaks centered around 1150-1170 nm, slightly red-shifted ($\sim$30 meV [2]) from the monolayer peak at approximately 1120-1135 nm. Exemplary RT PL spectra from the selected flakes are shown in Supplementary Fig. 1a. After identification, the flakes were transferred onto the substrate hosting the nanopillars using a transfer stage that heated the chip to 70 °C. At this temperature, the van der Waals interactions between the flake and the substrate overcome the adhesion to the PDMS, allowing the flake to release cleanly from the polymer. During this process, the flake conforms to the underlying nanopillar topography, creating directional nanowrinkles [3]. Finally, defects were introduced to the lattice by electron beam bombardment (JBX-9500FS, JEOL, 100 kV, 1000 µC/cm^2) of the strained areas.

The wafer consists of a substrate composed of alternating layers of AlAs and GaAs fabricated by low-pressure metalorganic vapor-phase epitaxy (MOVPE), forming a distributed Bragg reflector (DBR). The used layer pattern: 20 pairs of GaAs/AlAs on GaAs wafer with thickness of 85.0 nm/99.7 nm was optimized for high reflectivity in 1100-1200 nm range (more details in Supplementary Note S2). On top of the DBR, $\sim$100 nm of Al_2O_3 was fabricated by atomic layer deposition at 200 °C. Alignment marks and electrodes were fabricated by spin coating and patterning UV resist (nLOF 2020, AZ), followed by physical vapor deposition of a Ti/Au/Ti multilayer (5/50/5 nm) and a liftoff process. For the fabrication of the nanopillars, a small chip is cleaved from the wafer and spin-coated with a high-resolution negative e-beam resist (hydrogen silsesquioxane or HSQ, XR-1541-006, Dow Corning) at 3000 rpm for 1 min, followed by two baking steps at 120 °C and 220 °C, each for 2 minutes. The resist was patterned (JBX-9500FS, JEOL, 100 kV, 6 nA) with a dose of 11000 µC/cm^2 and developed in a 1:3 solution of AZ 400K : H_2O to obtain $\sim$100 nm tall nanopillars in the shape of a three-pointed star.

To enable electrical biasing, the $MoTe_2$ flake in both the encapsulated and unencapsulated devices is positioned so that it makes direct contact with one of the electrodes while remaining in close proximity to a second electrode without touching it. This configuration allows the two electrodes to be connected via a printed circuit board (PCB) to a voltage source for controlled bias application. The full architecture of an unencapsulated device is schematically illustrated in Supplementary Fig. 1b and 2a.

To fabricate the encapsulated devices, thin hexagonal boron nitride (hBN) flakes were first identified under an optical microscope (Nikon, 20× objective, NA = 0.45). An hBN flake was then transferred onto the substrate to serve as the bottom encapsulation layer. Subsequently,

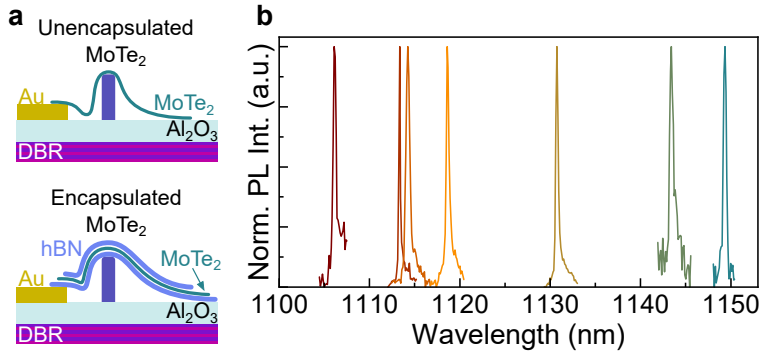

Supplementary Figure 2: **(a)** Schematic of the full sample architecture for unencapsulated (top) and hBN-encapsulated (bottom) devices. Both designs include a distributed Bragg reflector (GaAs/AlAs) substrate, an Al_2O_3 dielectric layer, and strain-inducing nanopillars. The $MoTe_2$ flake lies in contact with one gold electrode and in close proximity to a second one, for the application of bias. **(b)** Representative µPL spectra collected from encapsulated devices at T $\sim$ 4 K under 1080 nm CW excitation, displaying sharp emission lines between 1100 and 1150 nm.

the bilayer $MoTe_2$ flake was deposited, followed by the placement of an additional hBN flake on top to complete the encapsulation. The full stack of the sample is schematically presented in Supplementary Fig. 2a. Due to the rigidity of hBN, [4, 5], this approach results in less strain, forming a final structure consisting of bubble-like (rather than wrinkle-like) flake deformation. The modified strain and shape of the strained region can potentially significantly modify the properties of quantum emitters (QE), including the formulation of the emitters within the strain-driven hybridization of the defect states [6, 7]. Supplementary Figure 2b presents a range of narrow emission lines from multiple positions across the encapsulated sample, with wavelengths spanning from 1090 nm to 1160 nm, proving the possible generation of the QEs.

Supplementary Note 2: DBR perfomance.

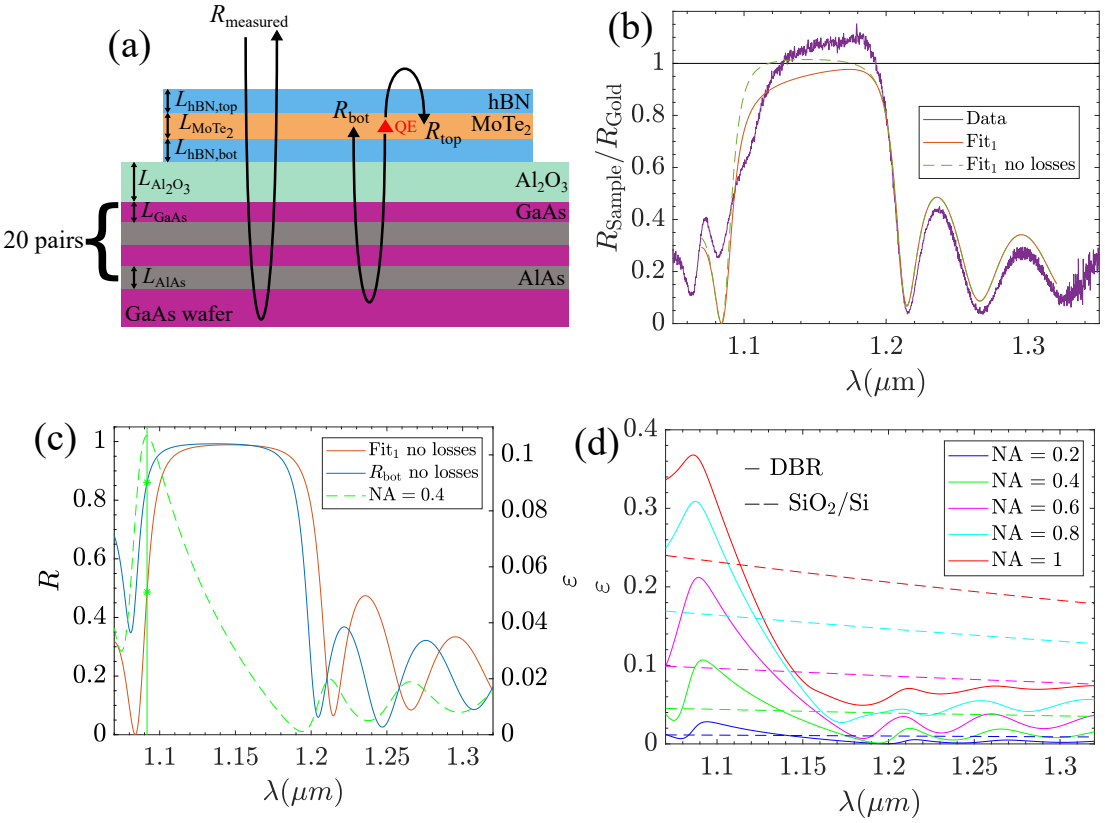

Supplementary Figure 3: **(a)** Sketch of the planar sample and a QE, indicated by the red triangle, positioned in the $MoTe_2$. The reflections are also indicated with arrows. **(b)** Normalized reflectivity as a function of the wavelength. The dark green dashed line shows the fitted result where the imaginary part of the refractive index of $MoTe_2$ is set to zero. **(c)** Left side: reflectivity as a function of the wavelength. The orange line is the dark green dashed line from (b); however, no longer normalized by the gold film. The blue line is the bottom reflectivity experienced by the QE. Right side: extraction efficiency for NA = 0.4 as a function of the wavelength. The vertical solid green line indicates the peak extraction efficiency. **(d)** Extraction efficiency as a function of the wavelength for various values of the NA. The solid lines are for the Al_2O_3/DBR structure and the dashed lines are for the SiO_2/Si structure.

In Figure 1b of the main text, we have presented measured reflectivity data at $T \sim 4\ K$ and simulated extraction efficiency. In this subsection, we aim to fit the measured reflectivity using a simple transfer matrix formalism. A sketch of the sample and the different thicknesses can be seen in Supplementary Fig. 3a. The measured data is normalized by measuring the reflectivity of a thin gold film. The simulated reflectivity is then also normalized by the simulated reflectivity of a thin gold film. To perform this task, we have used the following references for the refractive indices: GaAs ($T = 4K$) [8], AlAs ($T = 4$ K) [8], Al_2O_3 (room temperature) [9], hBN (room temperature) [10], $MoTe_2$ (room temperature) [11], and Au (room temperature) [12]. We note that the refractive index of several of these materials are only given at room temperature; however, this is the only available data to the best of our knowledge. The targeted layer thicknesses in the growth process were $L_{GaAs} = 85.0\,$nm, $L_{AlAs} = 99.7\,$nm, $L_{Al_2O_3} \approx 100\,$nm, 2 layers of $MoTe_2$, $L_{MoTe_2} = 1.64\,$nm, and approximately 7 layers of hBN below and above the $MoTe_2$, $L_{hBN,top/bot} = 2.8\,$nm. The number of DBR layer pairs is 20, followed by the GaAs wafer. In the fitting procedure, we allowed all thicknesses and refractive indices to change within certain limits. We place the following limits on the layer thicknesses: $L_{GaAs} \in [78.22, 91.82]$ nm, $L_{AlAs} \in [91.76, 107.71]$ nm, $L_{Al_2O_3} \in [70.00, 130.00]$ nm, $L_{MoTe_2} \in [1.56, 1.72]$ nm, and $L_{hBN,top/bot} \in [1.60, 4.00]$ nm. To change the refractive indices, we used the following simple model: $n_{x,fit}(\lambda) = s_x n_{x,data}(\lambda) + y_x$, where x refers to the material. We then applied the limits: $\{s_{GaAs}, s_{AlAs}, s_{Al_2O_3}\} \in [0.95, 1.05]$, $\{y_{GaAs}, y_{AlAs}, y_{Al_2O_3}\} \in [-0.1, 0.1]$, $\{s_{hBN}, s_{MoTe_2}\} \in [0.96, 1.04]$, and $\{y_{hBN}, y_{MoTe_2}\} \in [-0.05, 0.05]$. For $MoTe_2$, we fitted the

imaginary part independently from the real part: $k_{\mathrm{MoTe_2,fit}}(\lambda) = a_{\mathrm{MoTe_2}} k_{\mathrm{MoTe_2,data}}(\lambda) + z_{\mathrm{MoTe_2}}$, where we put the limits $a_{\mathrm{MoTe_2}} \in [0.96, 1.04]$ and $z_{\mathrm{MoTe_2}} \in [-0.05, 0.05]$. We then minimized the mean squared error (MSE) using fminsearchbnd in Matlab [13]:

$$\mathrm{MSE} = \frac{1}{N} \sum_{i=1}^{N} \left| \frac{R_{\mathrm{sample,measurement}}(\lambda_i)}{R_{\mathrm{Gold\ film,measurement}}(\lambda_i)} - \frac{R_{\mathrm{sample,calculated}}(\lambda_i, \mathbf{x}_{\mathrm{fit}})}{R_{\mathrm{Gold\ film,calculated}}(\lambda_i)} \right|^2, \tag{1}$$

where $\mathbf{x}_{\mathrm{fit}}$ includes all the mentioned fitting parameters. We obtain the following values in the fitting procedure: $L_{\mathrm{GaAs}} = 78.74$ nm, $L_{\mathrm{AlAs}} = 107.70$ nm, $L_{\mathrm{Al_2O_3}} = 71.91$ nm, $L_{\mathrm{MoTe_2}} = 1.61$ nm, $L_{\mathrm{hBN,top}} = 3.81$ nm, $L_{\mathrm{hBN,bot}} = 3.45$ nm, $s_{\mathrm{GaAs}} = 0.9978$, $y_{\mathrm{GaAs}} = -0.0724$, $s_{\mathrm{AlAs}} = 1.0114$, $y_{\mathrm{AlAs}} = -0.0166$, $s_{\mathrm{Al_2O_3}} = 0.9503$, $y_{\mathrm{Al_2O_3}} = -0.1000$, $s_{\mathrm{MoTe_2}} = 1.0041$, $y_{\mathrm{MoTe_2}} = 0.0459$, $s_{\mathrm{hBN}} = 1.0375$, $y_{\mathrm{hBN}} = 0.0499$, $a_{\mathrm{MoTe_2}} = 1.0288$, and $z_{\mathrm{MoTe_2}} = -0.0488$. The fitted curve is now shown in comparison to the measurement in Supplementary Fig. 3b. Overall, we observed decent agreement; however, the measured stop-band features a quite significant value above 1. We note that the fitted curve dips all the way down to zero to the left of the stop-band. We also included the simulated reflectivity, where we set the imaginary part of the refractive index of $MoTe_2$ to zero, i.e., no losses, which we will use in the following.

In Supplementary Fig. 3c, we then present the fitted reflectivity and the bottom reflectivity experienced by the QE, both without losses, against the simulated extraction efficiency for a numerical aperture (NA) of 0.4. The extraction efficiency is simulated by placing a classical point dipole in the center of the $MoTe_2$ layer, where the imaginary part of the refractive index of $MoTe_2$ is set to zero, as the model mentioned in the main text does not allow placing the dipole in a medium with a complex refractive index. Note that the simulated structure is entirely planar and, thus, the geometrical structuring of the wrinkles has not been taken into account. We note that the peak extraction efficiency is not at the center of the stop-band but at the left edge. It may appear as if the reflectivity has decreased at this point; however, the bottom reflectivity experienced by the QE is still high. The top reflectivity is mainly flat with a value of $R \sim 0.45$ due to the air interface. For increased NA, the peak extraction efficiency will blue-shift slightly further. This is due to larger contributions of light emitted at higher angles. The DBR stop-band, namely, blue-shifts with higher angles, causing this shift in the peak extraction efficiency. In Supplementary Fig. 3d, we compared the extraction efficiency of hBN encapsulated $MoTe_2$ on top of the Al_2O_3/DBR structure with simply placing hBN encapsulated $MoTe_2$ on top of a SiO_2/Si structure. The SiO_2 has a thickness of 115nm, and we use the following references for the refractive indices: SiO_2 (room temperature) [14] and Si ($T = 10$ K) [15]. We observe that the DBR causes an increased extraction efficiency around the emission of QEs in $MoTe_2$ at a wavelength of 1.1 µm compared to the SiO_2/Si structure. This showcases the benefits of the DBR structure. Additionally, we performed simulations of unencapsulated $MoTe_2$ on top of the DBR structure using the fitted parameters. Here, we observed an approximate decrease of $\varepsilon \sim 0.03$.

Supplementary Note 3: Broad excitonic peaks analysis.

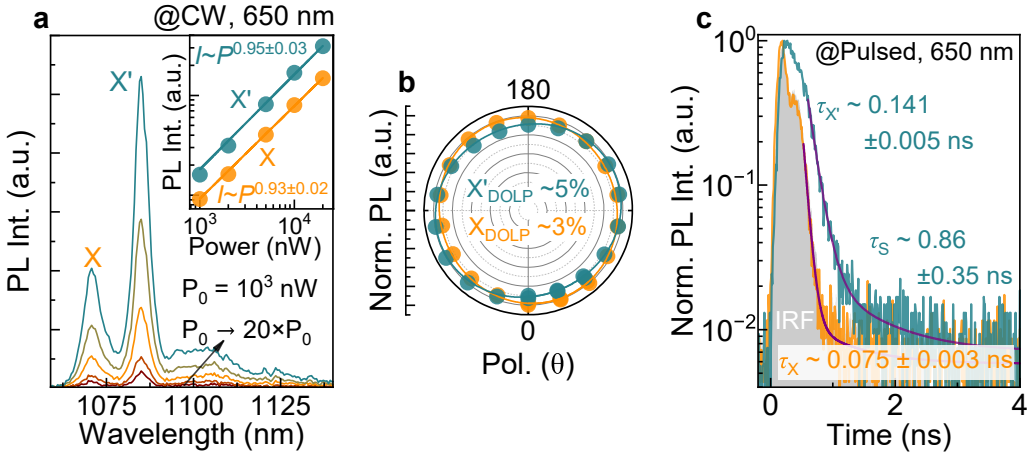

Supplementary Figure 4: **(a)** Power-dependent µPL spectra of the broad emission peaks X (orange) and X' (blue) presented in the main text. The inset shows the integrated peak intensity as a function of excitation power. Both peaks exhibit nearly linear behavior, with fitted exponents of ∼0.93-0.95, consistent with emission from basic excitonic complexes. **(b)** Polar plots of the maximum emission intensity versus polarization angle, yielding a low degree of linear polarization of ∼3-5%. **(c)** Time-resolved photoluminescence (TRPL) measurements of the X and X' peaks. For X, a mono-exponential fit gives a decay time $\tau_X = 75 \pm 3$ ps, close to the time resolution of the setup (gray area presenting instrument response function). For X', a bi-exponential fit reveals a fast component $\tau_{X'} = 141 \pm 5$ ps and a slower component $\tau_S = 0.86 \pm 0.35$ ns.

Supplementary Figures 4 and 5 include additional optical characterization data of the broad emission peaks observed in unstrained regions of the $MoTe_2$ flake, attributed to delocalized exciton recombination as discussed in the main text.

The power-dependent µPL spectra (Supplementary Fig. 4a) reveal nearly linear intensity scaling with excitation power, with exponents of ∼0.9–1, consistent with basic excitonic complexes. Polarization-resolved measurements (Supplementary Fig. 4b) show negligible anisotropy, with degree of linear polarization (DOLP) values below ∼0.06 for both peaks, further supporting their assignment to delocalized excitonic states.

Time-resolved PL measurements (Supplementary Fig. 4c) show very fast recombination dynamics, with extracted decay time below ∼150 ps ($\tau_X = 75 \pm 3$ ps, $\tau_{X'} = 141 \pm 5$ ps). In particular, the X peak exhibits a decay time of ∼70 ps, most likely limited by the temporal resolution of the setup. Such fast recombination is consistent with delocalized exciton emission and in line with previous reports of exciton lifetimes in the few-ps regime. [16] The X′ peak shows a slightly slower biexponential decay ($\tau_S = 0.86 \pm 0.35$ ns), which may indicate a weak contribution from localized states overlapping with the excitonic emission, or additional channels such as carrier trapping that influence the recombination dynamics.

The exact microscopic origin of the two peaks remains uncertain. At minimum, one expects to observe a neutral exciton peak, with a charged exciton feature emerging at lower energy depending on the local charge environment. Clarifying their origin requires further study and lies beyond the scope of this work.

The analysis of a second representative position in the sample (Supplementary Figure 5) revealed consistent signatures of delocalized excitonic recombination. In this case, a single dominant emission peak was observed, displaying a nearly linear power dependence of the PL signal, an even lower DOLP value (∼1%), and a faster recombination dynamics with a fitted lifetime as short as $\tau_X = 70 \pm 2$ ps. We note that the initial bump in the TRPL trace originates from the finite pulse shape of the excitation laser, as also illustrated by the instrument response function (IRF) included in the plot. These observations reinforce the assignment to delocalized excitonic transitions in $MoTe_2$, which exhibit markedly different properties compared to the localized quantum emitters analyzed in the main text.

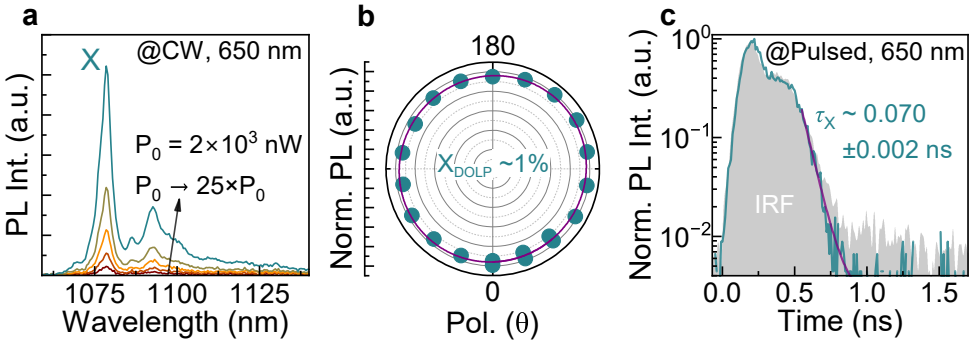

Supplementary Figure 5: **(a)** Power-dependent µPL spectra recorded under 650 nm CW excitation, showing the evolution of the excitonic peak (X) with increasing excitation power. **(b)** Polar plot of the emission intensity as a function of angle, yielding a degree of linear polarization (DOLP) of ∼1%, confirming the absence of polarization anisotropy. **(c)** Time-resolved photoluminescence (TRPL) measurement under 650 nm pulsed excitation. The monoexponential fit yields a decay time of $\tau_X = 70 \pm 2$ ps. The initial bump in the decay trace originates from the finite pulse shape of the excitation laser, as illustrated by the instrument response function (IRF) included in the plot.

Supplementary Note 4: Additional experimental data analysis of QE$_A$.

Supplementary Figure 6 presents additional optical characterization data for QE$_A$ described in the main text, including additional single-photon emission verification, emission stability characterization, and µPL measurements as a function of the sample temperature.

The Supplementary Figure 6a presents the same second-order autocorrelation measurement under CW quasi-resonant excitation as presented in the main text Fig. 2e, proving observation of single-photon emission. However, the significant bunching observation indicates limited internal quantum efficiency (IQE) to ∼0.66 at these experimental conditions. Additional measurement results for twice higher excitation power (P ∼ 1000 nW) revealed a slight reduction of the single-photon emission purity with a two times higher $g^{(2)}(0)$ fitted value of 0.11 ± 0.06 (Supplementary Figure 6b), likely connected to the stronger impact of the background emission. From the other side, higher excitation power modified the non-radiative processes, affecting the recombination dynamics, significantly reducing the amplitude and time of bunching observed in the autocorrelation measurement. Consequently, IQE increases from ∼0.66 to ∼0.81, close to the value observed in the case of CW above-band excitation presented in Fig. 2d within the main text. These results support findings related to the significant impact of the excitation condition on the recombination dynamics, especially non-radiative processes, likely connected to the charge environment fluctuations. The optimization of the excitation conditions, toward more resonant QEs addressing, could potentially improve both single-photon emission purity and the impact of other processes affecting recombination dynamics.

The mentioned charge noise also affects the QEs' emission stability in both energy and intensity due to spectral diffusion and charge-environment-dependent variation of excitation and recombination efficiency for a particular excitonic QE' transition. Supplementary Figure 6c presents the time trace of PL emission for QE$_A$ line for 150 s (integration time: 0.5 s). The statistical analysis of the linewidth revealed a value of 149±16 µeV, together with line wandering in the range of ∼150 µeV. The extracted line broadening support mentioned in the main text significantly limited spectral diffusion for the emitters investigated here, where the exact value can be overestimated by the limited spectral resolution of our setup (∼140-160 µeV). However, this value and statistic of the linewidth measured for more emitters (Supplementary Note S5) suggest still significant line broadening occurring here due to limited control of charge fluctuations within the QEs environment. The suggested more advanced excitation schemes, together with QE environment engineering, could potentially further reduce the effect of charge noise, reducing coherence of single-photon emission.

Besides the charge noise affecting the QEs' line broadening, there is also a crucial impact of the coupling between phonons and electrons (excitons), affecting also the coherence of single-photon emission, and limiting photon indistinguishability. Moreover, the potential of this process is strongly dependent on temperature, as the phonon distribution increases significantly

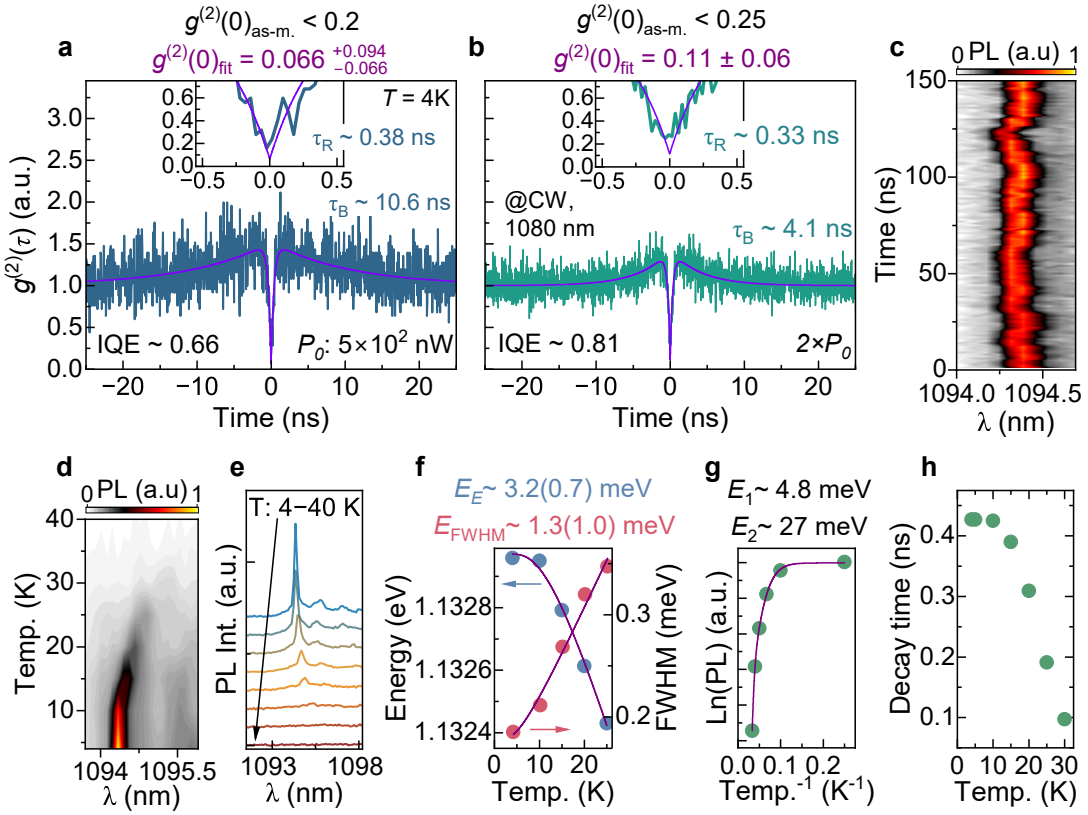

Supplementary Figure 6: **(a)** Second-order autocorrelation measurement under CW excitation at 1080 nm, yielding $g^{(2)}(0) = 0.066\ ^{+0.094}_{-0.066}$ and an internal quantum efficiency (IQE) of ~ 0.66. **(b)** Autocorrelation measurement of the same emitter at double the excitation power. The higher power modifies non-radiative processes, reducing the amplitude and timescale of bunching, which increases the IQE to ~ 0.81 but also raises $g^{(2)}(0)$ to 0.11 ± 0.06, thereby lowering the single-photon purity. **(c)** µPL time-trace recorded over 150 s (0.5 s integration time), revealing an average linewidth of 149 ± 16 µeV and spectral wandering of ∼150 µeV. **(d)** Intensity color map of QE_A emission as a function of temperature (4–40 K). **(e)** Corresponding µPL spectra at selected temperatures. **(f)** Extracted linewidth and central emission energy from fits to the spectra in (e). Both parameters show a redshift and broadening with increasing temperature. Fits yield average phonon energies of 3.2 ± 0.7 meV (energy shift) and 1.3 ± 1.0 meV (linewidth broadening), indicating a notable phonon contribution. **(g)** Emission intensity as a function of temperature. Fitting reveals two activation energies of ∼4.8 meV and ∼27 meV, indicating carrier escape from the localized state. **(h)** TRPL measurements from 4–30 K, showing a decrease in decay time from $>$ 400 ps at 4 K to $\sim$ 100 ps at 30 K, highlighting the growing role of non-radiative processes at elevated temperatures.

with temperature. Additionally, temperature-related crystal lattice modifications, together with phonons interacting with electrons, also affect QEs' energy emission. Finally, the non-radiative processes could also be strongly dependent on temperature, significantly reducing the radiative recombination efficiency. Supplementary Figure 6d-h presents the results of the analysis of the impact of temperature on QE_A emission properties. We observed QE_A emission up to 25-30 K with emission intensity decrease in the function of temperature (Supplementary Figure 6d,e). The analysis of the QE_A emission energy as well as line broadening (Supplementary Figure 6f) revealed a standard energy shift towards lower values, combined with an increase in the line broadening. Standard fitting of the average phonon energy for these two dependencies yielded 3.2 ± 0.7 meV for energy emission shift and 1.3 ± 1.0 meV for linewidth analysis. The obtained phonon average values close to single meV suggest a significant impact of the phonons at even low temperatures, in line with strong phonon-electron coupling observed for 2D TMD-based platform. The analysis of the QE_A emission intensity as a function of temperature (Supplementary Figure 6g) showed a fast emission intensity drop with two activation energies for carrier escape from the QE_A state. The fit yielded energy around 4.8 meV and 27 meV. These two

values can be connected to separate escape processes for electron and hole, or can also indicate the presence of some additional carrier trapping processes by local charge traps. Besides the nature analysis of observed emission quenching, the QE_A emission observation is strongly limited by the temperature. The reduction of charge traps surrounding QEs should potentially limit emitters' emission quenching by these additional states. However, the presence of these traps can be connected to the process of defect creation used in the formulation of the QEs, which is a rather crucial step in the sample preparation. Moreover, if the shallow confinement potential connected to weak localization is the limiting factor, then more advanced defects and strain optimization are needed to improve the confinement potential towards stronger localization of the carriers. Finally, the analysis of the recombination dynamics as a function of temperature (Supplementary Figure 6h) revealed a reduction of the decay time from above 400 ps to around 100 ps at 30 K, suggesting the impact of the non-radiative processes at elevated temperature. However, the lack of strong decay time changes up to 15 K can support a limited impact of the non-radiative recombination processes at low temperature ($T \sim 4$ K).

Supplementary Note 5: QEs parameters statistics.

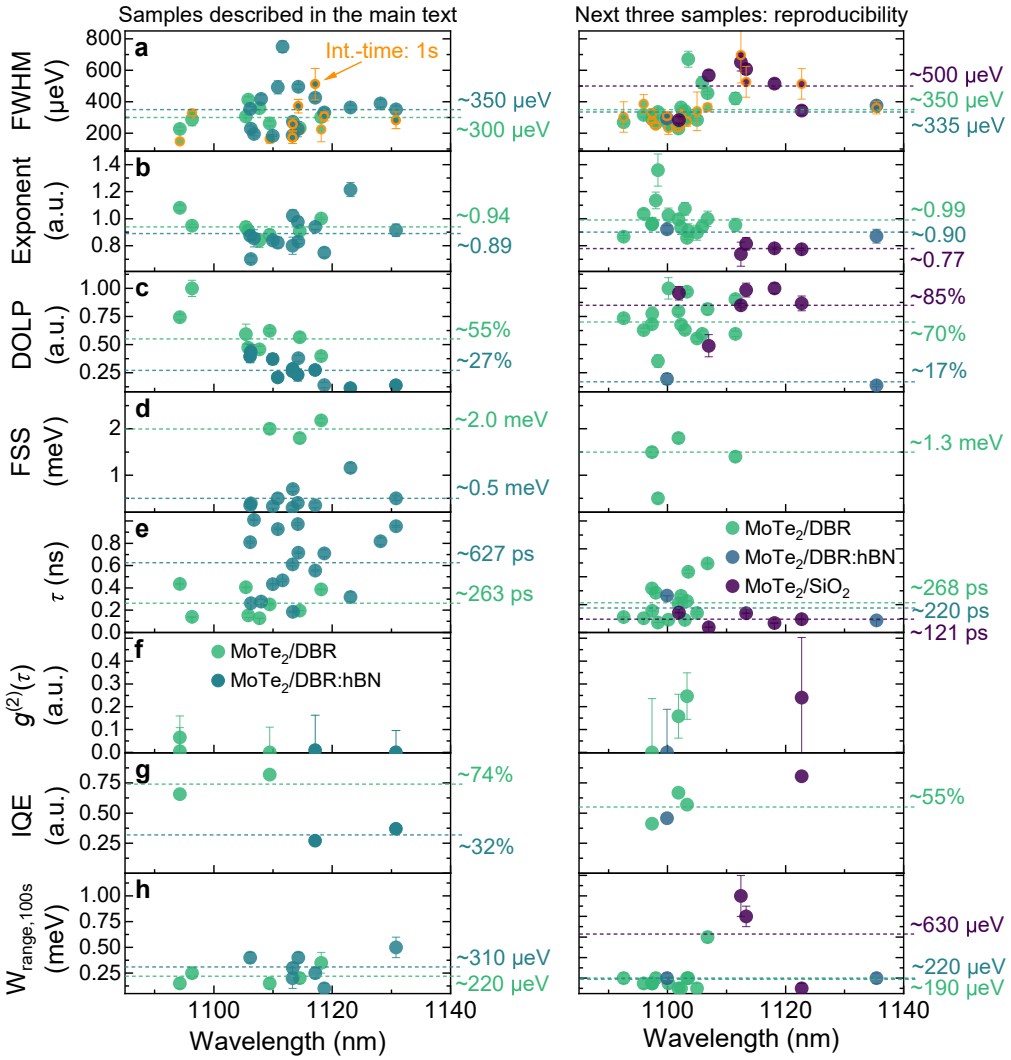

Supplementary Figure 7: Statistical analysis of key figures of merit for all emitters studied. Each panel displays results for the main sample set (left column) and for additional samples used to assess reproducibility (right column). Data points with an orange outline correspond to measurements with 0.5 or 1 s integration time, while all others use 10 s integration. Color coding indicates the sample type: light green (unencapsulated $MoTe_2$ on DBR), dark green (encapsulated $MoTe_2$ on DBR), and dark blue (unencapsulated $MoTe_2$ on SiO_2). All measurements were performed under CW 1080 nm excitation at 4 K. **(a–h)** Extracted average values of (a) FWHM, (b) power-law exponent, (c) degree of linear polarization (DOLP), (d) fine-structure splitting (FSS, when observed), (e) decay time, (f) $g^{(2)}(0)$, (g) internal quantum efficiency (IQE, when extractable), and (h) spectral wandering over 100 s. For each figure of merit, average values are reported both per sample set (left vs. right column) and per material configuration (color-coded categories).

To support the results presented in the main text, including identification of the quantum emitter properties, we analysed additional emitters in both unencapsulated and encapsulated flakes. Supplementary Figure 7 summarizes the optical properties characterization of all emitters, including linewidth, power-dependent QE intensity evolution, emission polarization anisotropy, fine-structure splitting (FSS), decay time, second-order autocorrelation, internal quantum efficiency, and the emitters' line-wandering analysis. Moreover, we reported the results obtained for three other samples investigated for the reproducibility of the quantum emitters (see Supplementary Note S8).

Specifically, we analysed the line broadening for all emitters (Supplementary Fig. 7a). We find comparable mean values of ∼300 μeV for unencapsulated emitters and ∼350 μeV for encapsulated

cases; however, a wider range of ∼185-750 µeV is found for encapsulated emitters compared to ∼230-420 µeV for unencapsulated emitters. For the other three samples, we found comparable linewidths with mean values ∼350 µeV and ∼335 µeV for the DBR substrate unencapsulated and encapsulated emitters, respectively, and slightly broader lines with a mean value of ∼500 µeV for the Si substrate. The SiO_2 layer on top of the silicon substrate is likely showing a higher impact of charge noise due to lower screening or a higher amount of charge traps surrounding emitters. However, the lower extraction efficiency observed in this case (Supplementary Note S2) and possibly slightly different conditions in the creation of the emitter (for example, strain) can affect the excitation power needed for analyzing the line broadening, thereby influencing the presented values. Moreover, we verified the linewidth of some emitters using shorter integration times (0.5 or 1 s). For some emitters (such as QE_A, whose line is ∼150 µeV), we observed less line broadening, especially for unencapsulated QEs found in the sample presented within the main text with a mean value ∼220 µeV. However, some of the lines revealed similar line broadening or even slightly higher values due to variation of the excitation conditions used for PL time-traces.

The analysis of the power-dependent QEs emission (Supplementary Fig. 7b) revealed values around 0.8-1.1 for almost all cases, a signature of the basic excitonic complexes. The slightly lower values for the Si substrate are likely related to the limited extraction efficiency of the emission, affecting the analysis of the power-dependent emission in the lower power regime.

The analysis of the degree of linear polarization (DOLP) for the investigated emitters (Supplementary Fig. 7c) showed higher values for unencapsulated emitters above 50% compared to encapsulated emitters showing values below 40%. The mean values ∼55% for the first DBR-based sample, ∼70% for the next sample, and ∼85% for the emitters on the silicon substrate indicate a strong impact of the wrinkle formulation when no hBN encapsulation is applied. Conversely, hBN encapsulation showed a direct way to reduce DOLP with a mean value of ∼27% for the first sample and ∼17% for the next sample. The obtained result can be related to a lower shape anisotropy of the strained region and to reduced wrinkle formation when additional hBN encapsulation is used. Coherently with these results, the FSS analysis (Supplementary Fig. 7d) revealed higher values for unencapsulated emitters (in the range of ∼0.5-2.2 meV) than hBN encapsulated emitters (in the range of ∼0.3-1.2 meV), supporting higher confinement potential anisotropy in the case of wrinkle-driven quantum emitters.

The analysis of the recombination dynamics (Supplementary Fig. 7e) revealed faster decays for the unencapsulated emitters within the first sample with a mean value of ∼263 ps, while the encapsulated emitters showed a mean value of ∼627 ps. The range of the decay in encapsulated emitters is wider, covering ∼190-1000 ps (unencapsulated emitters: ∼130-440 ps). These results can be explained by a different charge environment between these two cases, as described in the main text. The analysis of the time-resolved emission for the next samples showed similar fast decays in the case of the unencapsulated emitters with ∼268 ps mean values. The two encapsulated emitters revealed similar decay times (∼108 ps and ∼330 ps). Lack of more emitter characterization hindered verification of the difference in recombination dynamics between the unencapsulated and encapsulated cases. The decay values on Si-substrate sample were among the fastest, with a mean value of ∼121 ps and even below 100 ps for two cases. However, the limited intensity of the investigated emitters, application of the higher excitation power, and lower ratio between signal and background likely slightly impacted the obtained results and lowered the observed decay time values.

The second-order autocorrelation measurements (Supplementary Fig. 7f) confirmed the quantum nature of the emitters in all samples, with $g^{(2)}(0)$ being less than 0.5 in all emitters. In the first sample, both unencapsulated and encapsulated emitters showed fitted $g^{(2)}(0)$ values below 0.1, underlying observation of high-purity single-photon emission out of the investigated QEs. The next samples showed slightly less purity, most likely due to lower suppression of the background emission. The significantly limited performance of single-photon emission for QE on a silicon substrate can be linked to the application of higher excitation power to obtain sufficient coincidence counts within a reasonable time. The increased excitation power can reduce the $g^{(2)}(0)$ value due to both higher background emission and reduced recombination, where the initial decay time below 150 ps is relatively close to the setup resolution time. Short decay likely limits clear antibunching dip observation and forces the application of the reduced time bin values for better time resolution. Both low intensity of QE emission and reduced time-bin size reduce the speed of autocorrelation measurement accumulation. Besides the single-photon emission verification, the autocorrelation measurements enable the investigation of the impact of

non-radiative processes limiting the IQE (Supplementary Fig. 7g). We observed an IQE above 60% for unencapsulated QEs and below 50% for encapsulated emitters in the first sample, suggesting a higher impact of the charge-noise-driven non-radiative blinking in the encapsulated emitters. In the additional samples, we observed a similar level of IQE (40-70%) and a higher value for the silicon substrate-based sample, but with a rather limited amount of coincidences hindering the IQE verification.

Finally, the analysis of the line wandering (Supplementary Fig. 7h) showed similar values (100-400 µeV) of the line fluctuation within a spectral recording of 100 s (with 0.5 or 1 s integration time) from most of the emitters. The other samples showed slightly less wandering, possibly due to lower excitation power or the reduced impact of charge noise. The highest values observed for two emitters on the silicon substrate-based sample are likely connected to the application of the higher excitation power needed due to the lower extraction efficiency of the emission. However, it is also possible that reduced screening or a higher amount of charge traps surrounding emitters could also affect the observed line wandering.

Supplementary Note 6: QE$_A$ second-cooldown analysis.

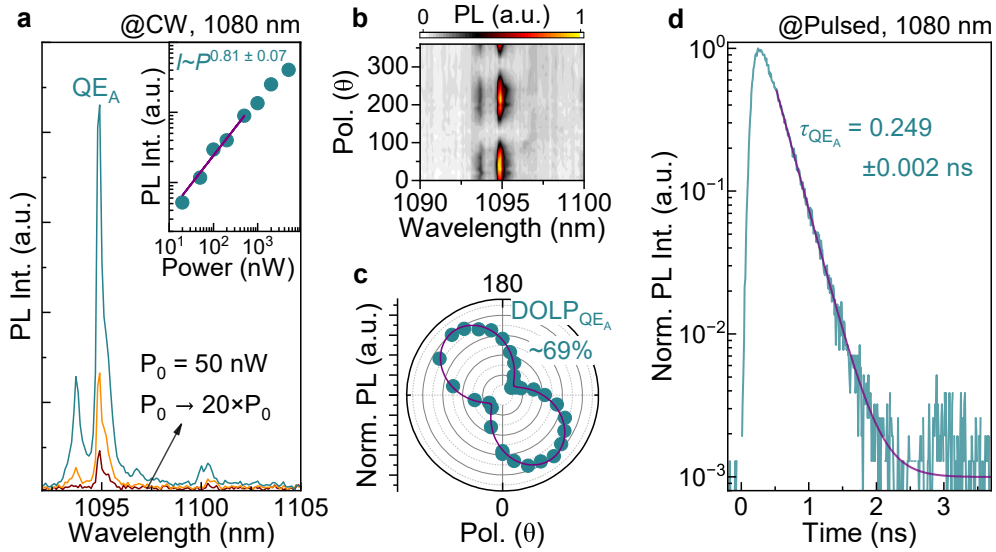

Supplementary Figure 8: **(a)** Power-dependent µPL spectra with the inset showing the extracted power dependence of the integrated intensity, yielding an exponent of 0.81 ± 0.07. **(b)** Polarization-resolved µPL intensity map as a function of analyzer angle (0–360°), displaying the characteristic polarization emission anisotropy of quantum emitters. **(c)** Polar plot of the maximum intensity against the polarization angle, with a fitted degree of linear polarization (DOLP) of ∼69%. **(d)** Time-resolved photoluminescence (TRPL) measurement under pulsed excitation, fitted with a monoexponential function, revealing a decay time of $\tau_{QE_A} = 249 \pm 2$ ps.

To further assess the QE$_A$ emission—and, in particular, the HOM experiment described in the main text—we carried out a second cooldown of the same sample. The second cooldown procedure is nontrivial, since warming up the sample back to room temperature and exposing it to the atmosphere can significantly alter the microscopic charge environment, disrupt the defect complexes responsible for the quantum emitters, or, in the worst case, permanently degrade the sample. The results of this second cooldown are presented in Supplementary Fig. 8 and 9, confirming the possibility to investigate QE$_A$ even with subsequent cooldowns and supporting the robustness of our platform.

In Supplementary Figure 8a, we provide optical spectra of QE$_A$ for a few excitation powers at the second cooldown. The power-dependent µPL analysis revealed a nearly linear dependence with an exponent of 0.81 ± 0.07, slightly lower than the value of 1.08 ± 0.02 extracted in the first cooldown (main text, Fig. 2b). Such a deviation may reflect subtle changes in carrier capture pathways or in the balance between radiative and non-radiative recombination channels induced by the altered charge environment. The polarization-resolved measurements (Supplementary Fig. 8b,c) remained consistent with the first cooldown, yielding a DOLP of 69% compared to 74% previously, confirming the emitter's robust polarization properties. However, the TRPL measurement (Supplementary Fig. 8d) revealed a pronounced reduction in lifetime, with $\tau_{QE_A} = 249 \pm 2$ ps compared to 440 ± 2 ps in the main text. This difference is consistent with changes in the local charge environment, which can strongly influence recombination dynamics. Notably, this effect aligns with our bias-dependent study in Fig. 4e of the main text, where the emitter lifetime decreased from ∼0.44 ns at 0 V to ∼0.25 ns at 15 V.

Supplementary Figure 9 shows the second-order autocorrelation measurements of QE$_A$ from the second cooldown. The extended-time-window histogram (±250 ns) under pulsed excitation (80 MHz) reveals a clear antibunching dip at zero delay (Supplementary Fig. 9b) with bunching ranging up to 300 ns time delay range, from which we extract an internal quantum efficiency of ∼0.64. A zoomed-in view of the central peak (within ±15 ns) highlights the antibunching behavior, with a fitted $g^{(2)}(0) = 0.342 \pm 0.016$ (Supplementary Fig. 9c). The observed coincidences around zero delay are likely related to the re-excitation process due to additional carriers provided to the emitter after the first radiative decay, probably from local defect traps surrounding the investigated emitter. The registered additional dip with the lowest value below

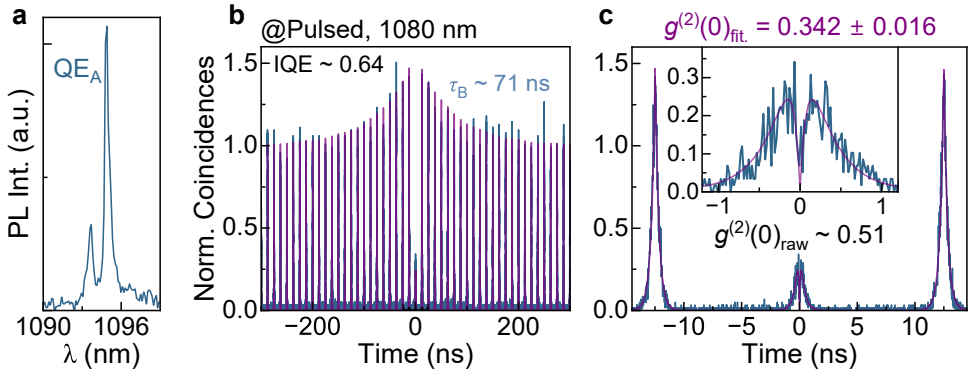

Supplementary Figure 9: **(a)** µPL spectrum under continuous-wave 1080 nm excitation at 4 K, showing the emission line of QE_A. **(b)** Second-order autocorrelation measurement $g^{(2)}(\tau)$ under pulsed excitation (80 MHz repetition rate) over an extended time window (±250 ns). The data exhibit a clear bunching, from which an internal quantum efficiency of ∼0.64 is extracted. **(c)** Zoomed-in view of the autocorrelation histogram around ±15 ns. The inset highlights the antibunching dip, with a fitted $g^{(2)}(0) = 0.342 \pm 0.016$, both confirming single-photon emission from QE_A.

$g^{(2)}(0) < 0.1$ exactly at zero delay supports these findings. These values confirmed that QE_A continues to operate as a stable single-photon emitter even after thermal cycling, demonstrating the robustness of our fabrication approach. The obtained higher $g^{(2)}(0)$ fitted value with a significant recapturing process affecting the purity of single-photon emission is likely related to increased excitation power needed for the subsequent HOM experiment. By contrast, the lower excitation power used for the $g^{(2)}(0)$ measurement presented in the main text (Fig. 2f) enabled higher single-photon emission purity.

Supplementary Note 7: Other unencapsulated QEs characterization.

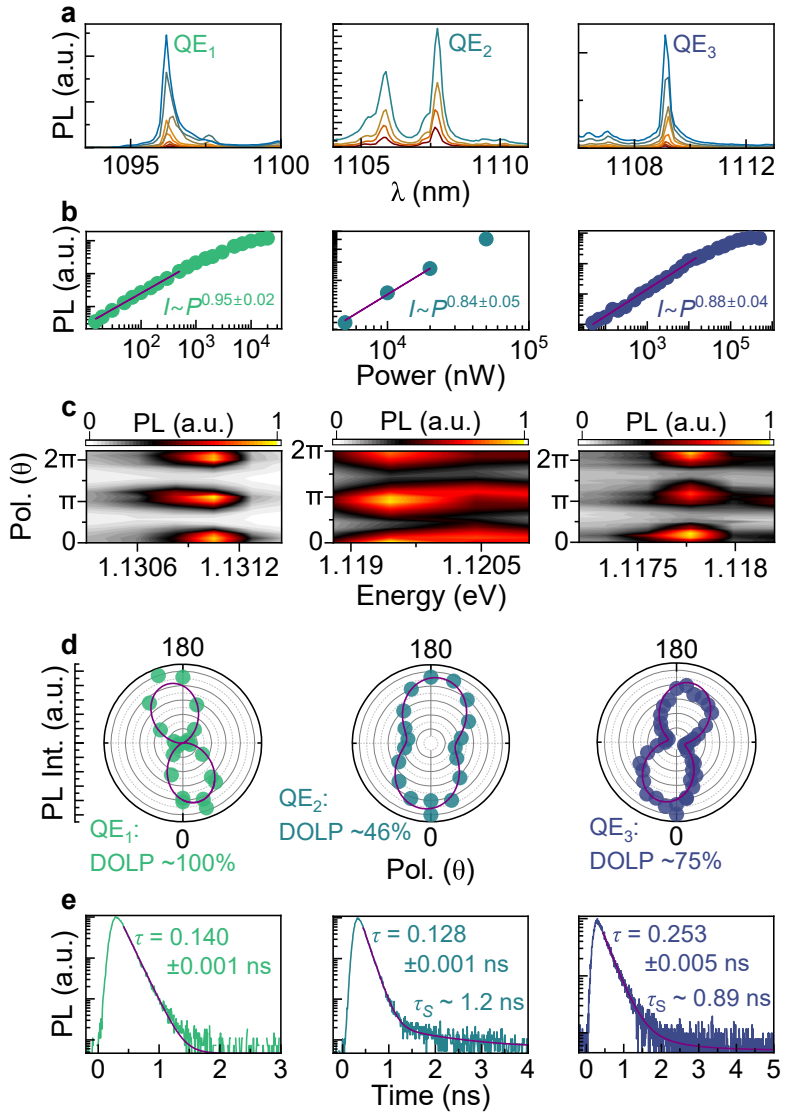

Supplementary Figure 10: **(a)** µPL spectra under different excitation powers (1080 nm CW excitation, $T = 4$ K), revealing sharp emission lines for three unencapsulated emitters (QE_1, QE_2, QE_3). **(b)** Power dependence of the peak intensity, with fitted exponents of 0.95, 0.84, and 0.88 for QE_1, QE_2, and QE_3, respectively. **(c)** Polarization-dependent emission maps as a function of analyzer angle, showing clear modulation for all three emitters. **(d)** Corresponding polar plots of the emission intensity, yielding degrees of linear polarization (DOLP) of 100%, 46%, and 75%. **(e)** Time-resolved photoluminescence (TRPL) measurements. QE_1 exhibits a monoexponential decay with $\tau \sim 140$ ps. QE_2 shows a biexponential decay with $\tau_{\text{fast}} \sim 128$ ps and $\tau_{\text{slow}} \sim 1.2$ ns. QE_3 also displays a biexponential decay, with $\tau_{\text{fast}} \sim 253$ ps and $\tau_{\text{slow}} \sim 0.89$ ns.

To support the results of the QE characterization in the main text, we characterized additional emitters within an unencapsulated flake structure, proving observation of similar optical properties (Supplementary Fig. 10) and single-photon emission (Supplementary Fig. 11) as in the main text.

Supplementary Figure 10a-e presents a set of optical characterization results for three similar emitters to QE_A, including power-dependent emission intensity characterization, polarization-dependent emission study, and time-resolved emission measurements. The power-law fits supported basic excitonic transitions verification in all cases (Supplementary Fig. 10b). Polarization-dependent characterization revealed significant confinement potential anisotropy with DOLP above 40% for all emitters (Supplementary Figure 10d). Recombination dynamics analysis

showed short decay times with two cases below 150 ps and one around 250 ps (Supplementary Figure 10e), Supplementary the observation of the fast recombination dynamics observed for QE_A presented in the main text and even indicating faster dynamics with decay times below 200 ps. The additional decay time component observed in two cases suggests additional non-radiative processes, such as carrier trapping near the emitter.

Supplementary Figure 11a presents additional verification of the single-photon emission for QE_3 under CW quasi-resonant (1080 nm) excitation at T $\sim$ 4 K. Clear antibunching observation at zero delay between two detectors supports single-photon emission observation with raw $g^{(2)}(0)$ value below 0.15 and fitted value $g^{(2)}(0) = 0.00\ ^{+0.12}_{-0.00}$. The slight bunching observation suggests blinking affecting IQE limited to $\sim$82%. The data were measured under additional +5 V bias conditions, which potentially affected the $g^{(2)}(0)$ value as well as IQE. Nevertheless, the data prove single-photon emission from QE_3. Moreover, Supplementary Figure 11b,c shows the time stability of QE_3 within 100 s (with 1 s integration time) for two power 5 µW and 100 µW. The statistical analysis of the linewidth revealed a value of 164$\pm$28 µeV, together with line wandering in the range of $\sim$150 µeV for lower excitation power (Supplementary Fig. 11b). The increased excitation power clearly increased line wandering to the range of about 300 µeV (Supplementary Fig. 11c) and also showed more frequently the events of the line fluctations, most likely due to increased charge noise at higher power of the laser.

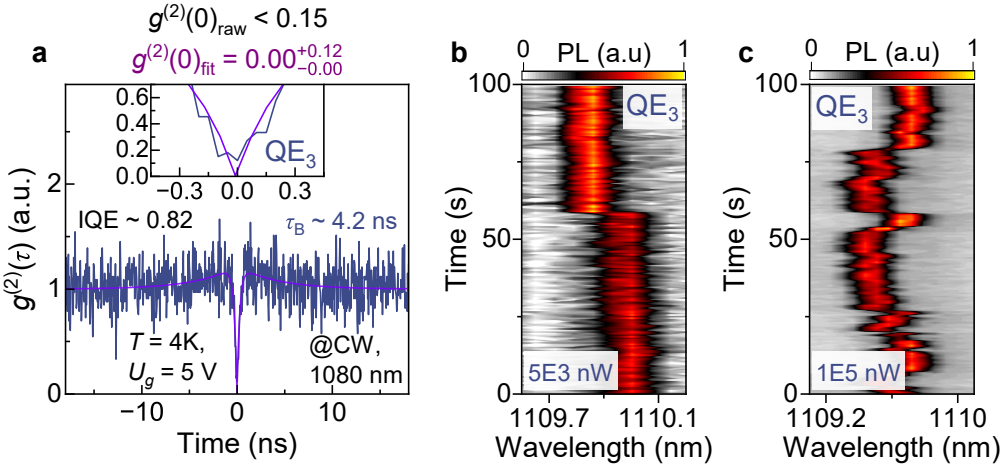

Supplementary Figure 11: **(a)** Second-order autocorrelation measurement under $V_g = 5$ V, 1080 nm CW excitation, and $T = 4$ K for emitter QE_3. The fitted value yields $g^{(2)}(0) = 0.00\ ^{+0.12}_{-0.00}$, with the raw value at zero delay below 0.15, confirming high single-photon purity and only minimal bunching. **(b)** PL time trace of QE_3 recorded under low excitation power (5×10^3 nW). The emission remains largely stable, aside from a discrete spectral jump around $\sim$60 s, after which the line stabilizes at a new central wavelength. **(c)** PL time trace under higher excitation power (1×10^5 nW). In this case, the emitter exhibits pronounced spectral wandering and instability.

Supplementary Note 8: Sample reproducibility.

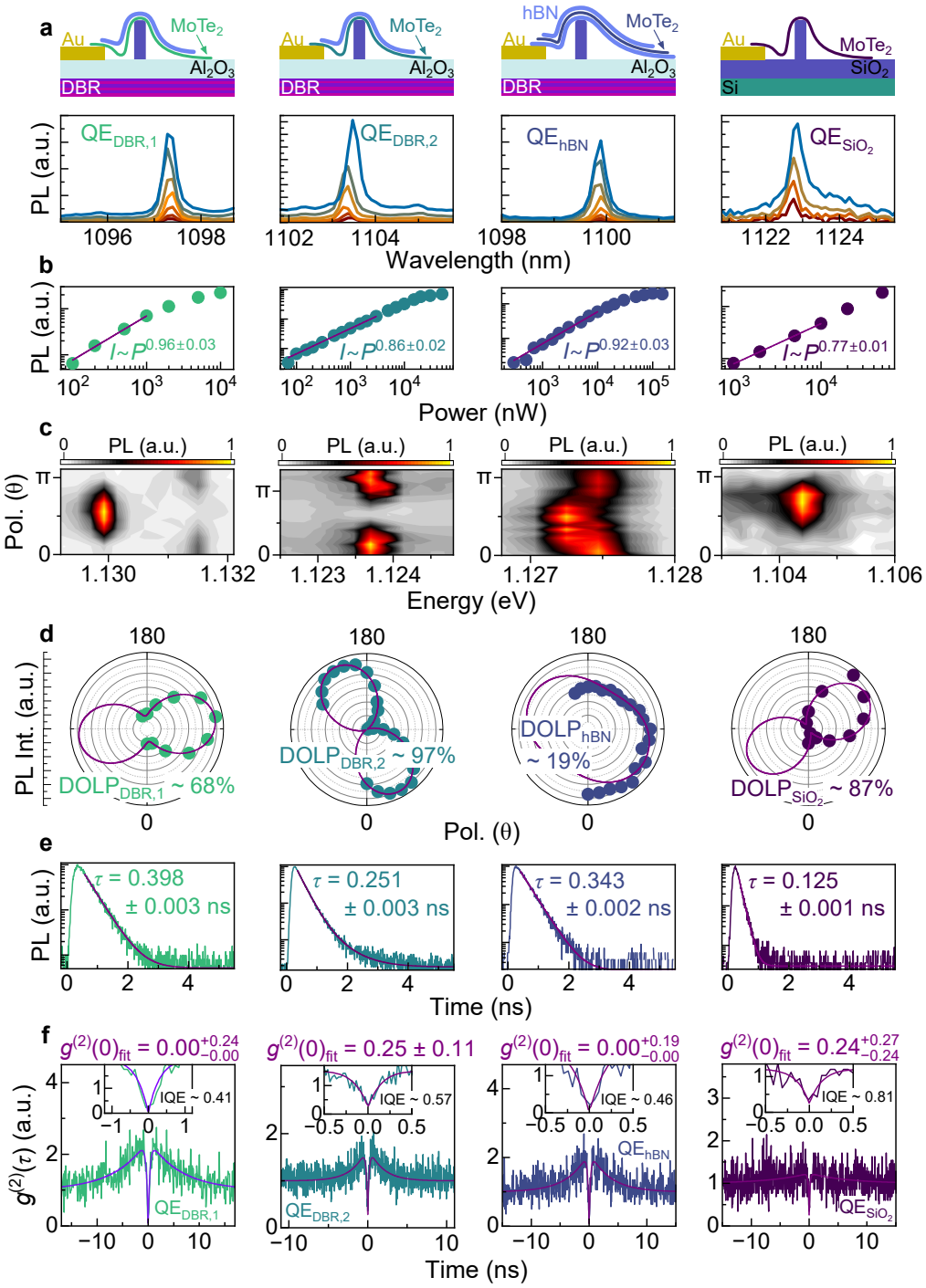

Supplementary Figure 12: Optical characterization of representative emitters from three batches. The first column corresponds to a batch fabricated with identical parameters to the main text sample (DBR/Al_2O_3 substrate, identical nanopillar geometry, and e-beam irradiation). The second and third columns correspond to a batch with increased nanopillar height, with exemplary emitters from both a top-encapsulated and an encapsulated flake, respectively. The fourth column shows data from a control batch fabricated on a Si/SiO_2 substrate. Rows show **(a)** PL spectra, **(b)** power dependence of the peak intensity with fitted exponents close to unity for all emitters, **(c)** polarization-resolved intensity maps, **(d)** extracted polarization plots with corresponding DOLP values (68%, 97%, 19%, 87%), **(e)** TRPL measurements with mono-exponential fits yielding lifetimes of 398 ps, 251 ps, 343 ps, and 125 ps, and **(f)** second-order correlation measurements confirming high single-photon purity across all samples.

To verify the reproducibility and robustness of our fabrication process, this Supplementary Note provides a systematic study of multiple sample batches with different fabrication parameters. The stability of the emitters under second cooldown was already demonstrated in Supplementary Note S6, confirming that emitter presented in the main text remain optically active and stable after exposure to the atmospheric environment.

The first reproducibility test was carried out on a sample fabricated using the exact same process as the sample presented in the main text, described in Supplementary Note 1. This included an identical DBR/Al_2O_3 substrate with both encapsulated (top or fully) and non-encapsulated $MoTe_2$ flakes transferred onto nanopillars, followed by e-beam irradiation with the same dose at wrinkle sites. The first column of Supplementary Figure 12 presents the full optical characterization of a representative top-encapsulated emitter from this batch (PL spectrum, power dependence, polarization dependence, lifetime, and $g^{(2)}(\tau)$). The results reproduce the behavior presented in the main text, confirming the validity of the process.

To understand the effect of strain engineering in the material, in the next batch we modified the nanopillar fabrication step by increasing their height to 300 nm (compared to ∼100 nm in the initial batch). For fully-encapsulated flakes, the transfer process proved more challenging due to the reduced conformability of the hBN layer, which could not fully adhere to the substrate surface. After transferring in that case, we applied additional thermal annealing to improve contact between the flake and the pillars. For top-encapsulated flakes, apart from occasional breakage during transfer, no substantial differences were observed. The second and third columns of Supplementary Figure 12 show the characterization of emitters from both fully-encapsulated and top-encapsulated flakes in this batch. Once again, typical single-photon emission behavior was observed. In the encapsulated case, the main deviation was a reduced DOLP compared to the unencapsulated emitters, while other metrics (lifetime, $g^{(2)}(\tau)$, power dependence) remained consistent. This behavior is likely linked to the inability of hBN to conform to the geometries and produce pronounced nanowrinkles, resulting in weaker one-dimensional strain potentials, which in turn reduce dipole alignment.

Finally, to rule out the possibility that the observed emission originates from QD-like centers in the DBR or Al_2O_3 material itself, we fabricated a control batch on a standard Si/SiO_2 substrate commonly used in the literature. The fourth column of Supplementary Figure 12 shows the corresponding optical data. As expected, the PL spectra exhibit a slightly reduced signal-to-noise ratio, which can be attributed to the lower extraction efficiency on a silicon substrate compared to the reflective DBR (see Supplementary Note S2). Nevertheless, the emitters in this batch also exhibit narrow emission lines with typical single-photon characteristics, confirming that the emission arises from engineered centers in the $MoTe_2$ flakes and not from substrate-related artifacts.

Together, these results demonstrate the reproducibility of our fabrication process across different batches and substrates. While variations in encapsulation and substrate choice can tune the polarization properties or extraction efficiency of the emission, the essential quantum emitter behavior remains consistent, validating the robustness and versatility of our approach.

Supplementary Note 9: Additional analysis of QEs in encapsulated flakes.

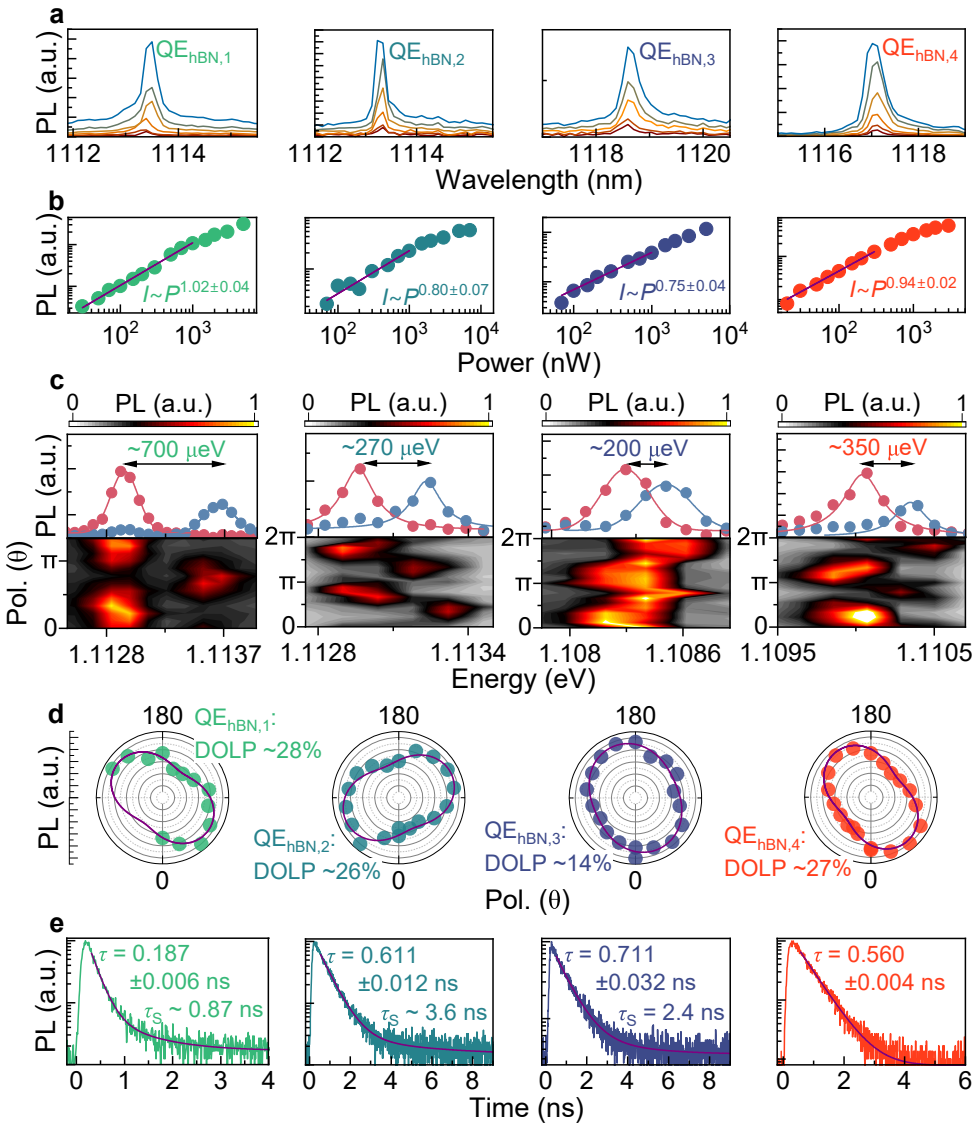

Supplementary Figure 13: Optical characterization of four encapsulated emitters ($QE_{hBN,1}$, $QE_{hBN,2}$, $QE_{hBN,3}$, $QE_{hBN,4}$). **(a)** PL spectra showing sharp emission lines. **(b)** Power-dependent emission intensity, with fitted exponents close to unity for all emitters. **(c)** Polarization-resolved measurements. Bottom panels: polarization-dependent intensity maps revealing pairs of emission lines with seemingly orthogonal polarization (except for emitter $QE_{hBN,3}$). Top panels: corresponding PL spectra of the lines with extracted fine-structure splitting values of 700, 270, 200, and 350 μeV. **(d)** Polar plots of the polarization dependence yielding DOLP values of 28%, 26%, 14%, and 27%. **(e)** Time-resolved PL measurements, with calculated lifetimes of 187 ps, 611 ps, 711 ps, and 560 ps. $QE_{hBN,1}$, $QE_{hBN,2}$, and $QE_{hBN,3}$ exhibit biexponential decay, with slower components pointing to additional non-radiative processes.

Supplementary Figure 13 and 14 provide additional results on the identification of encapsulated quantum emitters and verification of their single-photon emission, complementing the data presented in the main text (Fig. 3).

Supplementary Figure 13 presents data for the optical characterization of four emitters similar to QE_{hBN} ($QE_{hBN,1}$, $QE_{hBN,2}$, $QE_{hBN,3}$, $QE_{hBN,4}$), including PL spectra, power-dependent emission intensity, polarization-resolved emission revealing DOLP and fine-structure splitting (FSS), and time-resolved PL measurements. The PL spectra (Supplementary Fig. 13a) display sharp emission lines, while the power-dependent study (Supplementary Fig. 13b) confirms excitonic transitions in all cases, with exponents ranging between 0.75 and 1.05.

The polarization-dependent characterization reveals a reduced confinement potential anisotropy

for all encapsulated QEs, compared to the unencapsulated ones, with DOLP values below 30% (Supplementary Fig. 13d). In some emitters, we additionally observed pairs of emission lines with orthogonal polarization, consistent with fine-structure-split excitonic states (Supplementary Fig. 13c). The analysis of such correlated pairs showed FSS values ranging from 270 µeV to 700 µeV. In contrast to the other three emitters, the apparent line wandering observed for $QE_{hBN,3}$ mimicked FSS, but the absence of clear polarization dependence indicated that it could not be attributed to such a phenomenon.

The analysis of the recombination dynamics revealed longer decay times compared to unencapsulated emitters, with one case below 200 ps and three above 500 ps (Supplementary Fig. 13e). These results support the slower recombination dynamics observed for QE_{hBN} in the main text. In three cases, an additional decay component was observed, suggesting the presence of non-radiative processes such as carrier trapping near the emitter.

Supplementary Figure 14a presents additional verification of single-photon emission from $QE_{hBN,4}$ under CW quasi-resonant excitation (1080 nm) at T $\sim$ 4 K. Clear antibunching at zero time delay confirms the single-photon nature of emission. The raw $g^{(2)}(0)$ value is below 0.30, while the fitted result yields $g^{(2)}(0) = 0.01\ ^{+0.15}_{-0.01}$. The pronounced bunching around the dip indicates blinking, which limits the IQE to $\sim$27%. To compare the stability of emitter $QE_{hBN}, 4$ with the one discussed in the main text (QE_{hBN}), Supplementary Figures 14b,c present the PL time trace of both within 100 s and 150 s (with 0.5 s integration time), respectively. Statistical analysis yields slightly higher broadening for $QE_{hBN,4}$, with average linewidths of 510 ± 100 µeV (compared to 282 ± 53 µeV for QE_{hBN}), but with reduced spectral wandering of $\sim$250 µeV for $QE_{hBN,4}$ (compared to $\sim$500 µeV for QE_{hBN}).

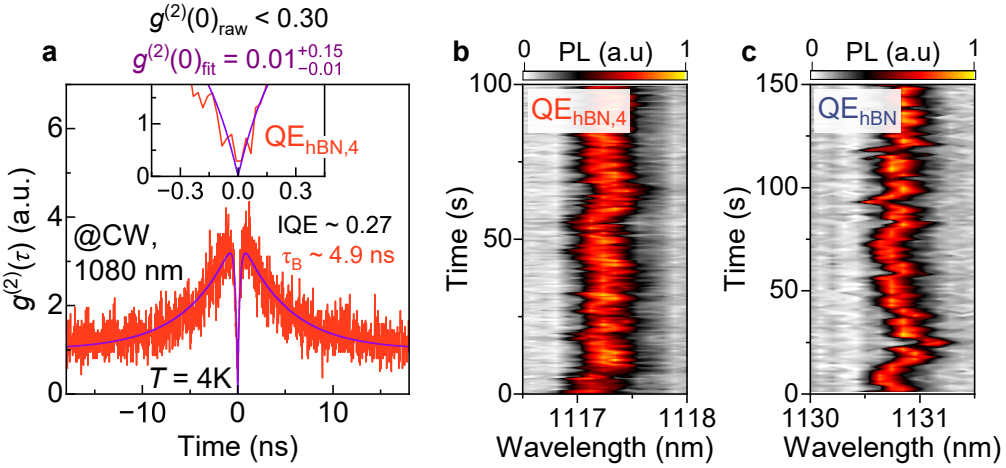

Supplementary Figure 14: **(a)** Second-order autocorrelation measurement of $QE_{hBN,4}$ under CW quasi-resonant excitation (1080 nm, T $\sim$ 4 K). Clear antibunching at zero delay confirms single-photon emission, with fitted $g^{(2)}(0) = 0.01^{+0.15}_{-0.01}$. Strong bunching indicates blinking, limiting the internal quantum efficiency (IQE) to $\sim$27%. **(b)** PL time trace of $QE_{hBN,4}$ over 100 s with 0.5 s integration. **(c)** PL time trace of QE_{hBN} (main text) over 150 s with 0.5 s integration. Both emitters exhibit significant line broadening (510 ± 100 µeV for $QE_{hBN,4}$ and 282 ± 53 µeV for QE_{hBN}) and spectral wandering above 200 µeV ($\sim$250 µeV for $QE_{hBN,4}$ and $\sim$500 µeV for QE_{hBN}).

Supplementary Note 10: Fine structure splitting analysis for unencapsulated QEs.

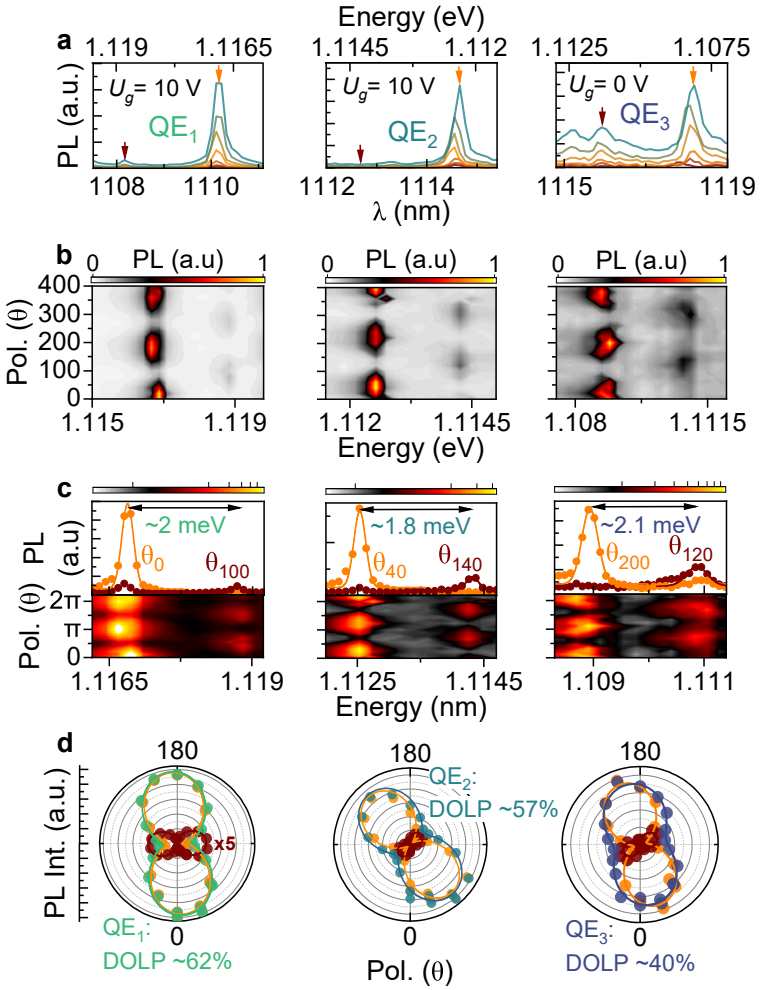

Supplementary Figure 15: Optical characterization of unencapsulated quantum emitters (QE_1, QE_2, QE_3) under no-bias (QE_3) and bias $V_g = +10$ V (QE_1, QE_2) conditions. **(a)** Representative PL spectra of all three emitters, highlighting the main emission line (orange arrow) and a weaker line of opposite polarization dependence (dark red arrow). **(b)** Polarization-resolved intensity maps showing strong linear polarization, indicative of anisotropic confinement potential. **(c)** Polarization analysis of the two lines for each emitter from panel (a), revealing orthogonally polarized dipoles with a FSS of 1.8–2.1 meV. **(d)** Degree of linear polarization (DOLP) analysis for the three emitters, yielding values above 30%.

To support the results presented in the main text and Supplementary Note S9 regarding the FSS characterization of encapsulated QEs, we performed additional investigation of the unencapsulated quantum emitters (Supplementary Fig. 15) to verify the FSS values for these emitters.

Supplementary Figure 15a-d presents a set of optical characterization results for three similar emitters to QE_A, focusing especially on the polarization-dependent emission anisotropies characterization affecting DOLP and also possible observation of the correlated pair of lines emitting in orthogonal polarization, suggesting observation of the two perpendicular dipoles separated by FSS. In accordance with wrinkle formulation for unencapsulated emitters, polarization-dependent characterization revealed significant confinement potential anisotropy compared to encapsulated emitters, showing strong linear polarization in the polar map (Supplementary Fig. 15b). However, in addition to the main line indicated by the orange arrow in the Supplementary Figure 15a, we also observed other weak lines (dark red arrow) separated from the main line showing opposite polarization dependence (Supplementary Fig. 15c), suggesting observation of the perpendicular dipole. The analysis of the energy separation revealed FSS values ranging

from 1.8 meV to 2.1 meV (Supplementary Fig. 15c). The much higher FSS values obtained here than in encapsulated cases (rather below 1 meV) support a much more anisotropic confinement potential, likely correlated with the wrinkles formulation. These funding additionally correlates with high values of DOLP above 30% for all emitters (Supplementary Fig. 15d), where the analysis of the polarization dependence for particular lines from the pairs indicates higher DOLP values as expected in the case of single dipole emission. The presented data proves the observation of similar optical properties for both encapsulated and unencapsulated QEs, showing both emission of the neutral complexes with measurable FSS values. However, in the case of the unencapsulated emitters, we observed indicated pairs of lines in two cases (QE_1 and QE_2) only for the emission registered under 10 V, while for QE_3, it was even possible without electrical biasing. The indicated need for electrical biasing to observe FSS can suggest the formulation of neutral excitonic complexes only under these conditions, supporting the identification of the observed step-like switching between two emission lines (see Supplementary Note S11) as a switching between neutral and charge excitonic complexes.

Supplementary Note 11: Electrical biasing.

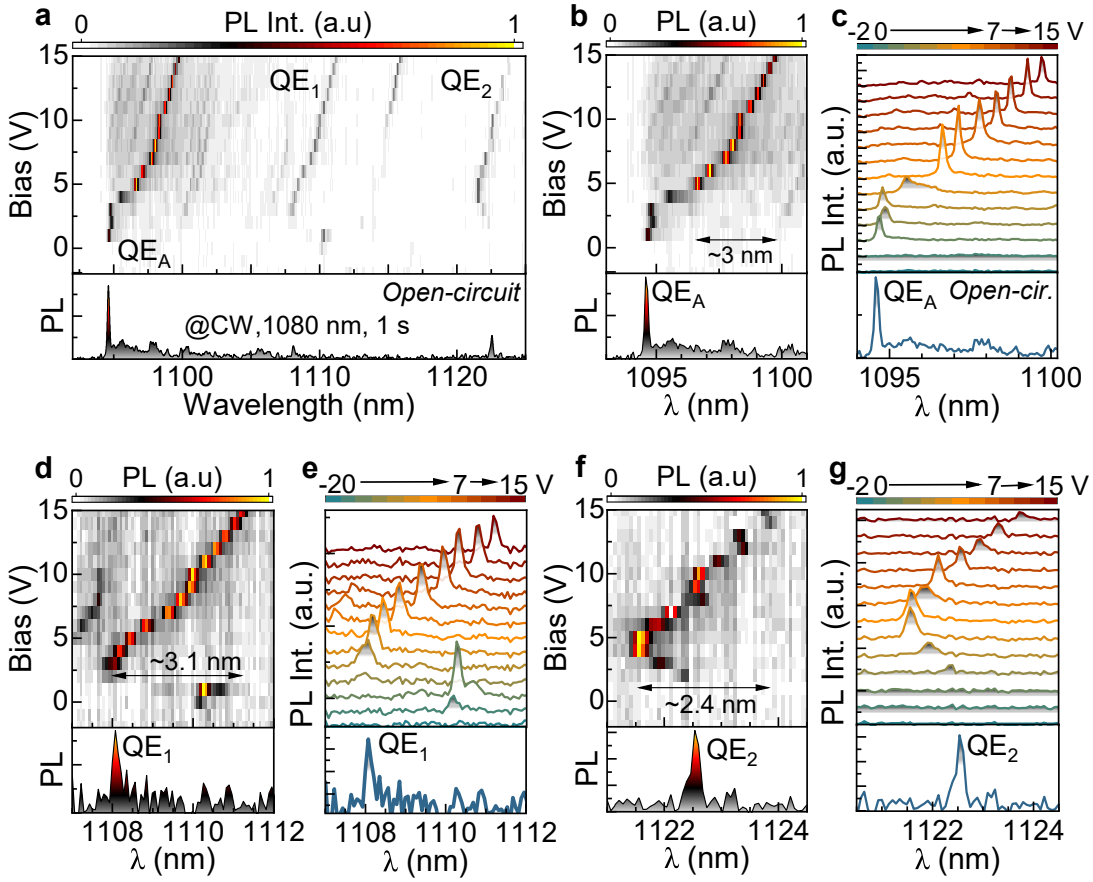

Supplementary Figure 16: **(a)** Long-range PL spectrum of the device at zero bias (CW excitation at 1080 nm, 1 s integration), overlaid with a bias-dependent PL heat map from -2 to +15 V, showing the evolution of three distinct emitters (QE_A, QE_1, QE_2). **(b)** Zoom-in on QE_A: the bottom panel shows the zero-bias PL spectrum, while the top panel presents the bias-dependent heat map, revealing a tuning range of ∼3 nm. **(c)** Open-circuit PL spectrum of QE_A compared to bias-dependent spectra acquired from –2 V to +15 V, confirming the Stark shift observed in (a,b). **(d,e)** Measurements for QE_1 equivalent to (b,c), showing a tuning range of ∼3.1 nm. **(f,g)** Measurements for QE_2 equivalent to (b,c), showing a tuning range of ∼2.4 nm. The emitter is quenched under negative bias, while under positive bias it initially blueshifts before redshifting beyond ∼5 V. The tuning range is defined as the maximum spectral separation between the most blueshifted and most redshifted positions of the emission lines.

Supplementary Figures 16 and 17 provide extended data and analysis of the electrical biasing of QE_A presented in the main text (Fig. 4b), as well as two adjacent emitters (QE_1, QE_2). These results confirm the Stark tuning of the emission energy under varying bias conditions and further explore how the applied field affects the optical properties of QE_A.

Supplementary Figure 16a presents a long-range bias-dependent intensity map highlighting the behaviour of all three emitters in the bias range between -2 and +15 V. They exhibit a clear Stark shift under positive bias (Supplementary Fig.16b–g), with tuning ranges of ∼3.0 nm, 3.1 nm, and 2.4 nm for QE_A, QE_1, and QE_2, respectively. This indicates that the applied bias directly modifies the confinement potential, thereby shifting the recombination energy. In addition to the gradual tuning, we observed a step-like switching behavior. For QE_A, spectra recorded at 3–5 V show a sudden transition from one emission line at 1094.5 nm to another at 1096.5 nm (energy separation ∼2 meV, Supplementary Fig. 16c). Such switching likely reflects a bias-induced change in the local charge environment that drives transitions between excitonic complexes. While the other two emitters showcase a switching-like behavior when transitioning from positive to negative bias values, we attribute this behavior to the stabilization of the system rather than an inherent excitonic transition.

Supplementary Figure 17 presents an analysis of the PL behavior of QE_A as a function of

bias. Supplementary Figure 17a focuses on a qualitative representation of how the PL intensity (top), linewidth (W_{exp}, middle), and emission energy (bottom) change under bias. The PL intensity increases by a factor ~ 6 around +7 V (10 s integration, orange points) compared to its unbiased value (orange line). Similarly, we notice a ~ 5 times increase at the same bias under 0.5 s integration, consistent with enhanced oscillator strength due to improved electron–hole wavefunction overlap. Another possible reason might be improved carrier capture or trap stabilization under bias. The linewidth remains nearly constant with applied bias, around 150 µeV for 0.5 s integration and 200–280 µeV for 10 s integration, with the discrepancy reflecting inhomogeneous broadening likely caused by charge noise. Above +4 V, the apparent broadening could be related to the aforementioned line-switching.

Finally, the emission energy shift extracted from both datasets (Supplementary Fig. 17a, bottom panel) yields a tuning range of ∼3 meV (∼3 nm), consistent with the Stark tuning observed in Supplementary Fig. 16.

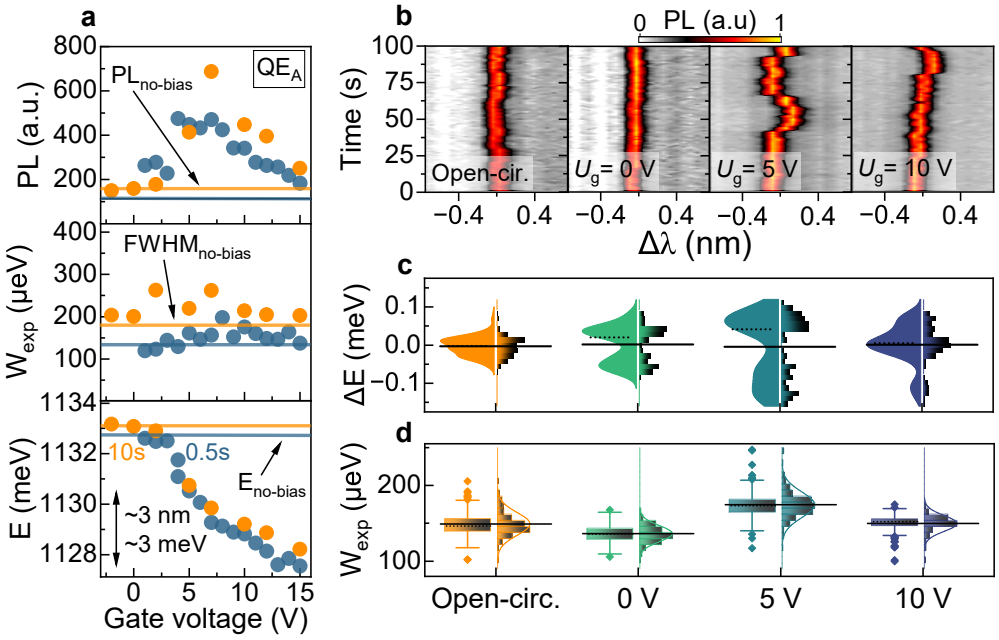

Supplementary Figure 17: **(a)** Bias dependence of the maximum PL intensity (top), linewidth (W_{exp}, middle), and emission energy (bottom) for QE_A, measured between –2 and +15 V. Two datasets are shown: 0.5 s integration (blue) and 10 s integration (orange). No-bias reference values are also indicated (coloured lines). The PL intensity initially increases with applied bias, reaching a maximum at $\sim$ 7 V, before decreasing again. The linewidth remains relatively stable at ∼200-280 µeV (orange) and ∼150 µeV (blue). The emission energy shows a clear Stark shift as a function of bias. **(b)** Time traces of the PL intensity (0.5 s integration) at open circuit, 0 V, +5 V, and +10 V, with a discernible increase in spectral wandering at +5 and +10 V. **(c)** Statistical analysis of emission energy fluctuations extracted from the time traces in (b), showing spectral wandering with mean values increasing from ∼100 µeV (open circuit) to ∼250 µeV (+5 V and +10 V). **(d)** Statistical analysis of the linewidth (W_{exp}) extracted from the time traces, with mean values around 140–180 µeV. The limited resolution of the setup (∼140–160 µeV) may influence the extracted values, potentially obscuring the intrinsic spectral width.

Moving to the statistical analysis of the PL behaviour, Supplementary Figure 17b presents time-trace PL measurements (100 s with 0.5 s integration time) for different biasing conditions (open circuit, 0 V, +5 V, and +10 V). We fitted every frame from the time-traces and assessed both the average spectral wandering (Supplementary Fig. 17c) and linewidth (Supplementary Fig. 17d) of the emission. We notice an increase in spectral instability from ∼100 µeV at zero bias to ∼250 µeV at +5 and +10 V. On the other hand, W_{exp} stays relatively stable around 140-180 µeV, close to the resolution limit of our setup (∼150 µeV), which prevents definitive conclusions on the intrinsic width. These results indicate that electrical biasing reduces the long-term stability of the emission. The effect is likely linked to random single-charge-trap

fluctuations in the local environment: while the applied field suppresses large-scale charge noise, it may also increase the emitter's sensitivity to the remaining local fluctuations. Overall, these findings reinforce the bias-induced tuning and stability effects discussed in Fig. 4 of the main text.

Supplementary Note 12: Two-photon interference data analysis.

To support the results presented in the main text regarding the indistinguishability characterization of QE_A, we present here more details of the data analysis of the Hong–Ou–Mandel (HOM) experiment (Supplementary Fig. 18). Additionally, we investigated the effect of the time-bin size reduction, lowering data resolution and noise, affecting the HOM experiment result. The normalization was carried out by averaging the peaks outside the bunching range through data fitting, including the peaks' height.

Supplementary Figure 18a,b illustrates the raw data obtained for co-polarized and cross-polarized configurations. In particular, we present the data in a wide range (±600 ns; Supplementary Figure 18a) to show the bunching effect already observed in the autocorrelation measurements (Supplementary Note S6). The average peak height outside the bunching range showed coincidence values of ~ 35 and ~ 47 for co- and cross-polarized data, indicated by dashed lines. For all the analyses presented later, we normalized the obtained data based on a broad data range fitting of the peaks' height out of the bunching range. Supplementary Figure 18b shows two magnified views of the data, highlighting the peaks around zero detuning (on the left) and an even more detailed view of the first peak (on the right).

To investigate the indistinguishability of the emitted photons for QE_A first, we performed analysis of the raw HOM data in a wide detuning range (±600 ns) recorded with a 20-ps time-bin size (Supplementary Fig. 18c) identical to the analysis presented in the main text. We fitted the co- and cross-polarized data according to Ref. [17], including also the bunching effect, using the following formulas:

$$\begin{aligned} C_{\mathrm{co}}(\tau) = A_{\mathrm{bg}} + \Bigg[& A_0 \cdot e^{-|\tau|/\tau_{\mathrm{dec}}} \left(1 - A_{\mathrm{ps}} e^{-|\tau|/\tau_{\mathrm{coh}}}\right) + A_{-1} \left(e^{-|\tau-\tau_0|/\tau_{\mathrm{dec}}}\right) \\ & + A_{+1} \left(e^{-|\tau+\tau_0|/\tau_{\mathrm{dec}}}\right) + A_{\mathrm{p}} \sum_{n\neq -1,0,1} e^{-|\tau+n\tau_0|/\tau_{\mathrm{dec}}} \Bigg] \\ & \times \left[1 + \left(\frac{\tau_{\mathrm{off}}}{\tau_{\mathrm{on}}}\right) \cdot e^{-\left(\frac{1}{\tau_{\mathrm{on}}} + \frac{1}{\tau_{\mathrm{off}}}\right)|\tau|}\right], \end{aligned} \tag{2}$$

for the co-polarized data and

$$\begin{aligned} C_{\mathrm{cross}}(\tau) = A_{\mathrm{bg}} + \Bigg[& A_0 \cdot e^{-|\tau|/\tau_{\mathrm{dec}}} + A_{-1} \left(e^{-|\tau-\tau_0|/\tau_{\mathrm{dec}}}\right) + A_{+1} \left(e^{-|\tau+\tau_0|/\tau_{\mathrm{dec}}}\right) \\ & + A_{\mathrm{p}} \sum_{n\neq -1,0,1} e^{-|\tau+n\tau_0|/\tau_{\mathrm{dec}}} \Bigg] \times \left[1 + \left(\frac{\tau_{\mathrm{off}}}{\tau_{\mathrm{on}}}\right) \cdot e^{-\left(\frac{1}{\tau_{\mathrm{on}}} + \frac{1}{\tau_{\mathrm{off}}}\right)|\tau|}\right], \end{aligned} \tag{3}$$

for cross-polarized data. A_{bg} represents background coincidences, A_0, A_{-1}, and A_{+1} captures the height of the center peak and two close side peaks, A_{ps} is amplitude of post-selected visibility, A_p is heigth of the other peaks out of the bunching range, τ_{dec} and τ_{coh} represents decay time and coherence time, $\tau_{\mathrm{on}}/\tau_{\mathrm{off}}$ are conected to observed bunching, τ_0 is related to the exciation pulsed laser repetition (12.5 ns). After the fitting and normalization, we integrated the area A_{co}, A_{cross} of the zero-detuning peaks in the 12.5 ns range for the co- and cross-polarized data. Using obtained values, we calculated the visibility as $V_{12.5\ \mathrm{ns}} = 1 - A_{\mathrm{co}}/A_{\mathrm{cross}}$. The analysis yielded a two-photon interference visibility of $10.6 \pm 4.2\%$ for QE_A.

To verify the potential statistics improvement and noise reduction through time-bin size increase, we also analyzed the data with a 40 ps time-bin size (Supplementary Fig. 18d). Based on the same method applied for raw data analysis (Supplementary Fig. 18c), we obtained only a slight two-photon interference visibility increase to $11.0 \pm 4.0\%$ for QE_A. Increasing the size of the time bin further increases the visibility value but limits the time resolution of the HOM data, hindering accurate fitting of the zero-detuning peak, especially in the post-selection range (range limited by the finite coherence time), showing an additional dip in co-polarized data. The final choice was a time bin of 20 ps, as its fitting arguably gave the best matching of co-polarized data, including the post-selection range fitting.

In conclusion, HOM experimental data revealed at least 10% two-photon interference visibility for QE_A in the 12.5 ns time integration window, together with even higher values observed by post-selection temporal filtering (Figure 5c in the main text). These results are, to the best of our knowledge, the first reported indistinguishability value for a $MoTe_2$-based quantum emitter.

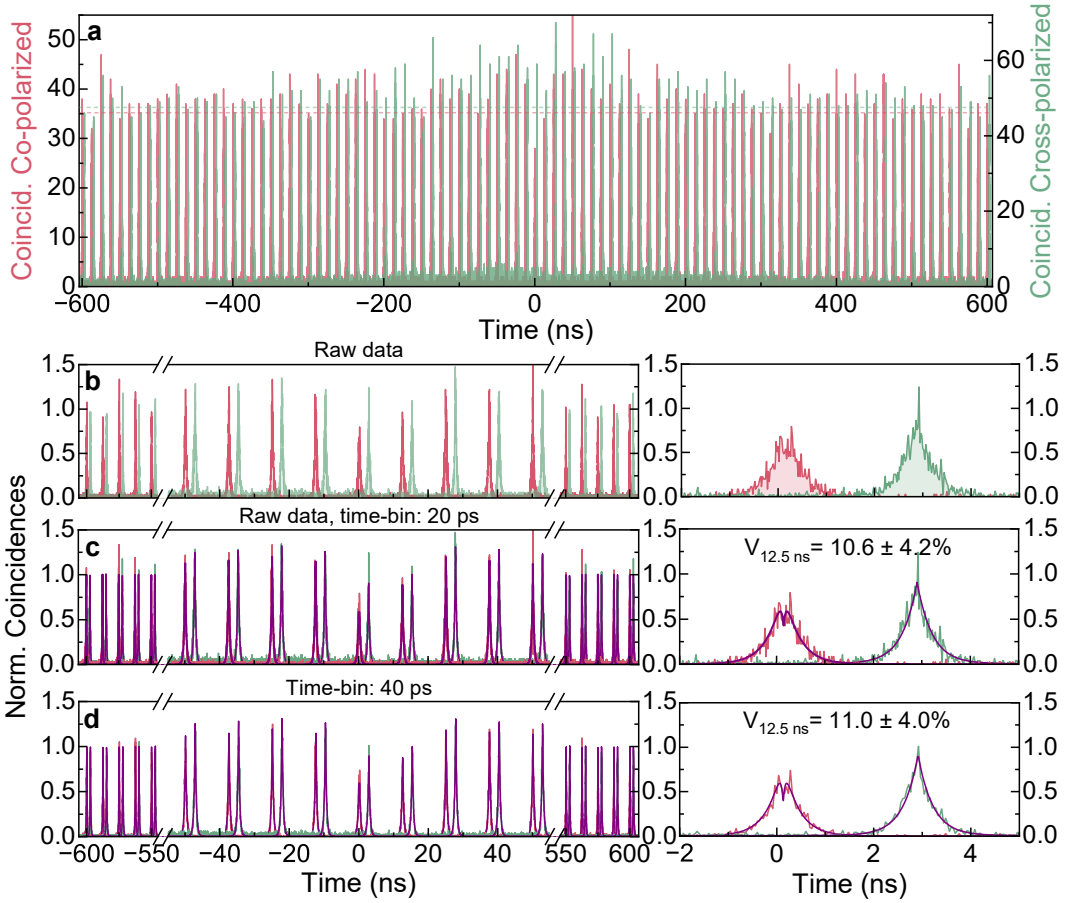

Supplementary Figure 18: Additional raw data from the two-photon interference experiment. **(a)** Raw data of the two-photon interference for co-polarized (red line) and cross-polarized (green line) photons, presented in two separate scales with slightly time-shifted cross-polarized data for better visual distinction. **(b)** Magnified views of the normalized raw HOM data around the zero-detuning value. **(c)** Raw two-photon interference data with 20 ps time-bin width analysis through direct fitting over ±600 ns range, including bunching. A comparison of the integrated coincidences in a 12.5 ns time integration window for both configurations indicates $V_{12.5\ \mathrm{ns}} = 10.6 \pm 4.2\%$. **(d)** Similar analysis of the HOM data with reduced 40 ps time-bin size showing $V_{12.5\ \mathrm{ns}} = 11.0 \pm 4.0\%$ for the integrated coincidences in 12.5 ns time integration window.

References

[1] Castellanos-Gomez, A. *et al.* Deterministic transfer of two-dimensional materials by all-dry viscoelastic stamping. *2D Mater.* **1**, 011002 (2014).

[2] Ruppert, C., Aslan, B. & Heinz, T. F. Optical Properties and Band Gap of Single- and Few-Layer $MoTe_2$ Crystals. *Nano Letters* **14**, 6231–6236 (2014).

[3] Paralikis, A. *et al.* Tailoring polarization in WSe_2 quantum emitters through deterministic strain engineering. *npj 2D Mater. Appl.* **8**, 59 (2024).

[4] Androulidakis, C., Zhang, K., Robertson, M. & Tawfick, S. Tailoring the mechanical properties of 2D materials and heterostructures. *2D Mater.* **5**, 032005 (2018).

[5] Daveau, R. S. *et al.* Spectral and spatial isolation of single tungsten diselenide quantum emitters using hexagonal boron nitride wrinkles. *APL Photonics* **5**, 096105 (2020).

[6] Linhart, L. *et al.* Localized Intervalley Defect Excitons as Single-Photon Emitters in WSe_2. *Phys. Rev. Lett.* **123**, 146401 (2019).

[7] Parto, K., Azzam, S. I., Banerjee, K. & Moody, G. Defect and strain engineering of monolayer WSe_2 enables site-controlled single-photon emission up to 150 K. *Nat. Commun.* **12**, 3585 (2021).

[8] Gehrsitz, S. *et al.* The refractive index of $Al_xGa_{1-x}As$ below the band gap: Accurate determination and empirical modeling. *J. Appl. Phys.* **87**, 7825–7837 (2000).

[9] Zhukovsky, S. V. *et al.* Experimental Demonstration of Effective Medium Approximation Breakdown in Deeply Subwavelength All-Dielectric Multilayers. *Phys. Rev. Lett.* **115**, 177402 (2015). URL `https://link.aps.org/doi/10.1103/PhysRevLett.115.177402`.

[10] Grudinin, D. V. *et al.* Hexagonal boron nitride nanophotonics: a record-breaking material for the ultraviolet and visible spectral ranges. *Mater. Horiz.* **10**, 2427–2435 (2023).

[11] Munkhbat, B., Wróbel, P., Antosiewicz, T. J. & Shegai, T. O. Optical Constants of Several Multilayer Transition Metal Dichalcogenides Measured by Spectroscopic Ellipsometry in the 300–1700 nm Range: High Index, Anisotropy, and Hyperbolicity. *ACS Photonics* **9**, 2398–2407 (2022). URL `https://doi.org/10.1021/acsphotonics.2c00433`.

[12] Ciesielski, A. *et al.* Evidence of germanium segregation in gold thin films. *Surf. Sci.* **674**, 73–78 (2018).

[13] D'Errico, J. fminsearchbnd, fminsearchcon. `https://www.mathworks.com/matlabcentral/fileexchange/8277-fminsearchbnd-fminsearchcon` (2024).

[14] Malitson, I. H. Interspecimen Comparison of the Refractive Index of Fused Silica∗,†. *J. Opt. Soc. Am.* **55**, 1205–1209 (1965).

[15] Franta, D. *et al.* Temperature-dependent dispersion model of float zone crystalline silicon. *Appl. Surf. Sci.* **421**, 405–419 (2017).

[16] Robert, C. *et al.* Excitonic properties of semiconducting monolayer and bilayer $MoTe_2$. *Phys. Rev. B* **94**, 155425 (2016).

[17] Vajner, D. A. *et al.* On-Demand Generation of Indistinguishable Photons in the Telecom C-Band Using Quantum Dot Devices. *ACS Photonics* **11**, 339–347 (2024).